Investigation of the physical and superconductivity properties of Ni$_3$AC (A: Mg, Zn and Cd)
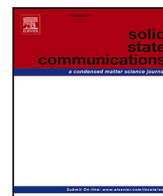
Zafer, T.; Kurtuluş, F.; Salimov, R.; Karaca, E.

Important note
To cite this publication, please use the final published version (if applicable).
Please check the document version above.

Full length article

Investigation of the physical and superconductivity properties of Ni₃AC (A: Mg, Zn and Cd)

T. Zafer [a,b,*], F. Kurtuluş [c], R. Salimov [d], E. Karaca [d,e,f]

[a] *Vocational School of Health Services, Sakarya University, 54050, Sakarya, Turkey*
[b] *Department of Materials Science and Engineering, Delft University of Technology, 2628 CD Delft, The Netherlands*
[c] *Sakarya Uygulamalı Bilimler Üniversitesi, Arifiye Meslek Yüksekokulu, 54580, Arifiye, Turkey*
[d] *Sakarya University, Faculty of Sciences, Department of Physics, 54050, Sakarya, Turkey*
[e] *Department of Physics, University of York, York YO10 5DD, United Kingdom*
[f] *Center for Advanced Laser Techniques, Institute of Physics, 10000 Zagreb, Croatia*

ARTICLE INFO

ABSTRACT

This study investigates the electronic and superconducting properties of Ni₃AC (A: Mg, Zn, and Cd) antiperovskites through first-principles computational methods. Importantly, Ni₃MgC has been identified as a superconductor with a transition temperature (T_c) of 8.644 K, while Ni₃ZnC and Ni₃CdC exhibit T_c values of 2.172 K and 3.861 K, respectively, in remarkable agreement with experimental. The electron–phonon interaction strength in these materials suggests medium-coupling superconductivity. This study provides significant insights into the mechanisms driving superconductivity in metal-carbide antiperovskites, identifying opportunities for their use in advanced technologies.

1. Introduction

Antiperovskites, usually referred to by the formula X₃BA, where X is a cation and A and B are anions of differing sizes, display atypical properties, including superconductivity and superionic conductivity, giving them suitable for various applications [1–3]. In 2001, He et al. discovered the new superconductor MgCNi₃, with a transition temperature of around 8 K to the superconducting state [4]. This discovery led to increased interest in Ni-based antiperovskite compounds. These compounds are known for their high Ni content, which suggests that magnetic interactions might be an important factor in their superconducting behavior. We also allowed for the emergence of magnetic properties in the Ni₃AC (A: Mg, Zn, and Cd) materials, but no evidence for spin polarization was found. AlCNi₃ [5] and ZnCNi₃ [6] have been synthesized by substituting Mg with Zn and Al in the superconducting intermetallic perovskite MgCNi₃, yet superconductivity has not been observed in any compound. Experimental results for ZnCNi₃ suggest that it has a lower density of states at the Fermi level compared to MgCNi₃. The decrease in the density of states could explain why ZnCNi₃ has a transition temperature around 2 K [6]. The synthesized CdCNi₃ suggested superconductivity at around T_c = 2.5-3.2 K, confirming the theory related to the density of states [7]. The mechanical and superconducting properties of ZnNNi₃, MgNNi₃, and CdNNi₃ are proven

in a first principle study by Chong Li et al. [8], which explains the roles of Zn, Mg, and Cd components in density of states .

Antiperovskite metal-carbides with the formula Ni₃AC (A = Cd, Mg, Zn, Al, Ga, and In) have attracted considerable attention due to their exceptional mechanical properties, including high ductility and strength [5,7–13]. Among these, Ni₃CdC is a known superconductor with a transition temperature (T_c) of 3.4 K [7]. Additionally, the mechanical stability of ZnCNi₃ and CdCNi₃ under high-pressure conditions has been explored [14]. Numerous studies have been conducted to explore the origins of superconductivity in the intermetallic antiperovskite Ni₃MgC [15]. Lin et al. [16], examined its low-temperature specific heat and suggested that Ni₃MgC follows moderate-coupling BCS behavior. The Eliashberg approach was also used to investigate the thermodynamic parameters of the superconducting antiperovskites CdCNi3 and MgCNi3, and, revealing that they exhibit medium and strong coupling, respectively [17–19]. In contrast, Singer et al. [20] investigated the nuclear spin-lattice relaxation rate, finding that Ni₃MgC behaves as an isotropic s-wave superconductor in the weak coupling regime, with a coherence peak below its critical temperature (T_c) of 7 K. Using DFT calculations, Shim et al. [21] identified Ni-3d states near the Fermi level as crucial to the properties of the material. They reported that Ni₃ MgC has a prominent and narrow peak in the density of states near the Fermi level, in contrast to Ni₃MgB and Ni₃MgN,

---

and proposed that the superconducting behavior in Ni_3MgC can be adequately explained by the conventional phonon mechanism. In this study, we investigate the electronic and superconductivity properties of Ni_3AC (A: Mg, Zn, and Cd). The purpose of this study is to understand the mechanism behind its superconductivity for each compounds.

2. Theory

Plane-wave periodic density functional theory codes on Quantum Espresso are applied for quantum mechanical approaches [22,23]. Generalized gradient approximation (GGA) parametrization has been used to compute the exchange–correlation functional. The interaction of the valence electrons with ionic cores is modeled by ultrasoft pseudopotentials [24]. The energy cutoff for plane wave expansions is set to 60 Ryd. The solution of Kohn–Sham equations [25] have been achieved by considering a set of Monkhorst–Pack special k points [26]. The structural characteristics of the compound are determined using a ($20 \times 20 \times 20$) k -mesh, while the electronic structure calculations are done by a denser ($24 \times 24 \times 24$) k-mesh. In electronic structure calculations, a more denser k-mesh is required compared to geometric optimization, as it ensures accurate sampling of electronic wavefunctions in k-space, which is essential for determining accurate band structures and electronic properties.

The phonon properties of these materials have been utilized using the linear response method [22,23]. Brillouin-zone (BZ) integration was achieved for phonon calculations using the $4 \times 4 \times 4$ Monkhorst–Pack k-points. We started by generating ten dynamical matrices corresponding to the Monkhorst–Pack grid $4 \times 4 \times 4$. Then, using Fourier transformation, they are transformed into real space, generating force constants that could be used to define phonon frequencies for any q-points. This methodology allows the calculation of the electron–phonon interaction and, then, the determination of T_c. The electron–phonon interaction has been explored using the linear response theory method within the framework of the Migdal–Eliashberg theory as follows [27,28]

$$\gamma_{\mathbf{q}j} = 2\pi\omega_{\mathbf{q}j} \sum_{\mathbf{k}nm} |g_{(\mathbf{k}+\mathbf{q})m;\mathbf{k}n}^{\mathbf{q}j}|^2 \delta(\varepsilon_{\mathbf{k}n} - \varepsilon_F)\delta(\varepsilon_{(\mathbf{k}+\mathbf{q})m} - \varepsilon_F), \quad (1)$$

where the relevant electron–phonon matrix elements $g_{(\mathbf{k}+\mathbf{q})m;\mathbf{k}n}^{\mathbf{q}j}$ which govern this interaction, have been accurately estimated through self-consistent calculations employing the linear response theory [22,23].

The Eliashberg spectral function($\alpha^2F(\omega)$) can be defined in terms of the phonon linewidth $\gamma_{\mathbf{q}j}$ of mode j at wavevector $\mathbf{q}$ by

$$\alpha^2 F(\omega) = \frac{1}{2\pi N(E_F)} \sum_{\mathbf{q}j} \frac{\gamma_{\mathbf{q}j}}{\hbar\omega_{\mathbf{q}j}} \delta\left(\omega - \omega_{\mathbf{q}j}\right), \quad (2)$$

where $N(E_F)$ corresponds to the electronic density of states at the Fermi level. The electron–phonon coupling constant has the following form

$$\lambda_{\mathbf{q}j} = \frac{\gamma_{\mathbf{q}j}}{\pi\hbar N(\varepsilon_F)\omega_{\mathbf{q}j}^2}. \quad (3)$$

The total electron–phonon coupling constant λ and logarithmically averaged frequency $\omega_{\ln}$ can be obtained from the integration of the Eliashberg spectral function.

$$\lambda = \int_0^\infty \frac{\alpha^2 F(\omega)}{\omega} d\omega \quad (4)$$

$$\omega_{ln} = exp\left(2\lambda^{-1} \int_0^\infty \frac{d\omega}{\omega} \alpha^2 F(\omega) ln\omega\right). \quad (5)$$

The value of superconducting transition temperature T_c can be obtained from the Allen–Dynes modified McMillan formula [29,30].

$$T_c = \frac{\omega_{\ln}}{1.2} \exp\left(-\frac{1.04(1+\lambda)}{\lambda - \mu^*(1 + 0.62\lambda)}\right), \quad (6)$$

where μ^* points out the screening Coulomb pseudopotential, frequently having a value between 0.10 and 0.16 [29,30]. We set μ^* as 0.13 in this study.

3. Computational results

3.1. Structural, electronic and fermi surface properties of Ni_3AC

Ni_3AC (where A represents Mg, Zn, and Cd) crystallizes in a cubic structure characterized by the space group $Pm\overline{3}m$ (No. 221) and has 5 atoms per unit cell. The atomic positions in the Wyckoff positions are as follows: Ni atoms are located at (0.5, 0, 0), A atoms at (0.5, 0.5, 0.5), and C atoms at (0.0, 0.0, 0.0). The crystal structure of Ni_3AC (A: Mg, Zn and Cd) is shown in Fig. 1. The geometric optimization is used to determine the structural properties of Ni_3AC. Ab initio calculations are utilized to achieve structural optimization, aiming for minimum total energy and zero force on atoms to obtain lattice parameter, equilibrium volume and bulk modulus. The calculated values of the lattice parameters for Ni_3AC (A: Mg, Zn and Cd) are determined as 3.822, 3.754, and 3.843 Å, which are excellent agreement with previous results [6,7]. The our theoretical results for Ni_3MgC, Ni_3ZnC, and Ni_3CdC show excellent agreement with recent experimental data, with deviations of just 0.31%, 2.5%, and 1.07%, respectively.

An in-depth analysis of the electronic band structure and density of states (DOS) is crucial for understanding the properties of conductivity and superconductivity. Fig. 2 shows the electronic properties of cubic Ni_3AC (A: Mg, Zn and Cd), showcasing the band structure along with Γ -X-M-R-Γ-M in the Brillouin zone, the total and partial density of states (DOS and PDOS) and the Fermi surface. The electronic band structures of Ni_3AC (A: Mg, Zn and Cd) reveal two bands crossed the Fermi level, indicating their metallic nature. A critical analysis of total and partial density of states in detail, shown in Fig. 2, shows that while the filled portion of the electronic density of states is divided into two sections by a gap for Ni_3MgC, Ni_3ZnC and Ni_3CdC is split into three regions. The lowest energy regions are dominated by the mixture of both s states of Ni and C atoms for each compound. This is to be expected since the low-energy levels are mostly filled with s states. Fig. 2 illustrates the total and partial density of states for Ni_3MgC. In the energy range of $-7.2 < E < -3.5$ eV, a strong hybridization between C 2p and Ni 3d states is clearly observed. The dominance near Fermi level for Ni_3MgC is primarily attributed to the Ni 3d states, with minor contributions from C 2p states. Fig. 2(b) differentiates from Fig. 2(a) with high peak in energy range of $-8 < E < -6$ which is under the dominance of Zn 3d states. In the energy range of $-5.3 < E < -3.8$ eV, a strong hybridization between C 2p and Ni 3d states is clearly observed. The major contribution near Fermi level for Ni_3MgC is primarily attributed to the Ni 3d states, with minor contributions from C 2p states. The similarity of the total and partial density of states in valence and conduction bands between Ni_3ZnC and Ni_3CdC can be seen from Fig. 2(b) and Fig Fig. 2(c) including the peak behavior in low energy region. The Fermi level plays crucial role to understand the mechanism of superconductivity. The value of N(E_F) plays a key role in superconductivity since the electron–phonon coupling parameter (λ) varies linearly with N(E_F), as described by the McMillan–Hopfield expression [29]:

$$\lambda = \frac{N(E_F)\langle I^2 \rangle}{M\langle \omega^2 \rangle} \quad (7)$$

where $\langle\omega^2\rangle$ represents the average squared phonon frequency, $\langle I^2 \rangle$ is the average squared electron–phonon matrix element, and M is the average atomic mass. We determined that the electronic density of states at the Fermi energy, N(E_F), is 4.88, 3.91 and 4.52 states/eV for Ni_3MgC, Ni_3ZnC and Ni_3CdC, respectively. From these values, we can infer that the critical temperature (T_c) of Ni_3MgC is higher compared to the other materials.

Fig. 2 suggests that the most important contribution to the formation of Cooper pairs of Ni_3AC (A: Mg, Zn and Cd) which governs the transition from metallic to superconducting states come from the Ni 3d states.

Figs. 2(a-c) shows the Fermi surfaces for Ni_3MgC, Ni_3ZnC and Ni_3CdC, respectively, based on the GGA calculations for the two bands
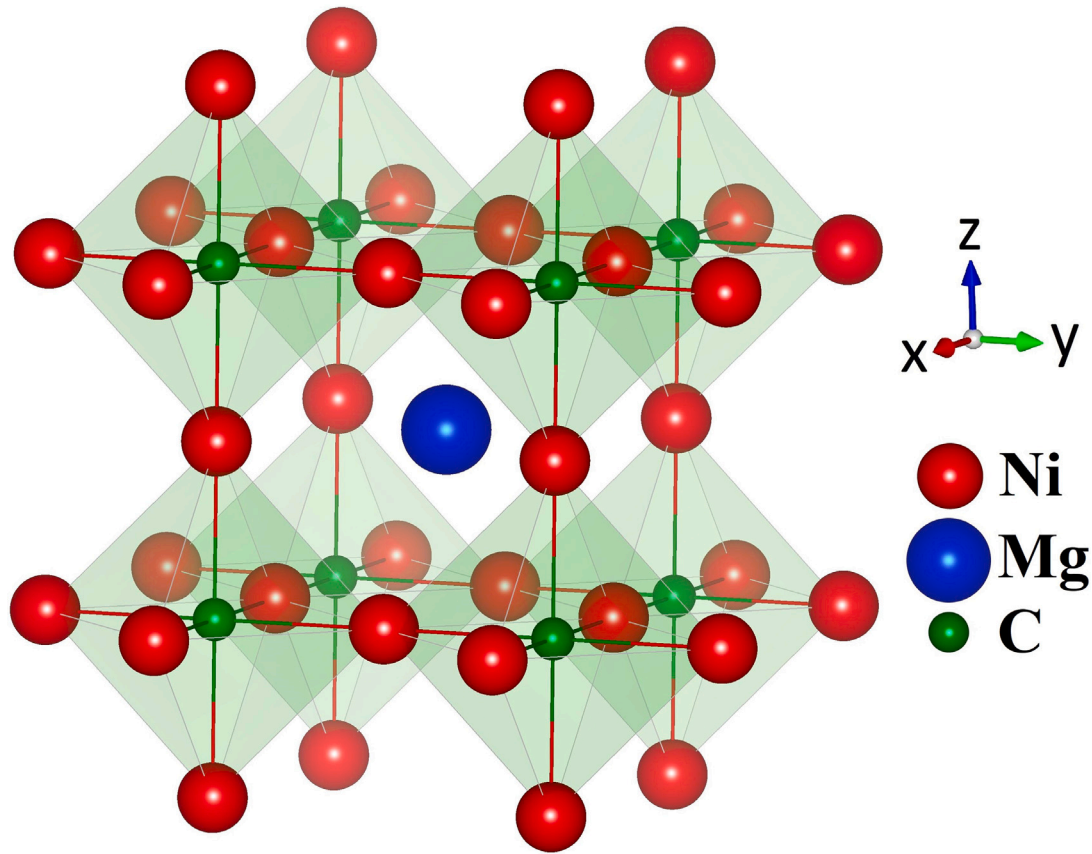
Fig. 1. Antiperovskite crystal structure of Ni_3AC (A: Mg, Zn and Cd).

crossing the Fermi level. The topologies of the Fermi surfaces are quite similar for Ni_3MgC, Ni_3ZnC and Ni_3CdC when Nickel is present in all three compounds. This similarity is likely due to the significant influence of the d-states from Nickel near the Fermi level, which plays a similar role in all these materials. Fig. 2 shows two bands that cross the Fermi level. The lower band, near the X point, forms a complex heavy sheet with an octahedral cage-like structure and a thin along the $R − M$ direction. On the other hand, the upper band creates a Fermi surface with two sheets, consisting of flattened square shapes centered around the X point that transform into ovoids as they approach the high-symmetry path from Γ to R.

The electron charge density plays a crucial role in understanding the nature of chemical bonding and the transfer of charge between ions when atoms come together to form a compound. We calculated the charge density to understand the nature of the chemical bonding, as shown in Fig. 3. The charge density maps for Ni_3MgC, Ni_3ZnC and Ni_3CdC illustrate significant variations in the electron density distribution around the central atoms (Mg, Zn, Cd). In Ni_3CdC, the Cd atom shows a high degree of localized electron density, suggesting stronger metallic bonding, while Ni and C atoms display overlapping charge densities indicative of covalent bonding. In Ni_3ZnC, the Zn atom also exhibits a high electron density, though it is slightly less localized compared to Cd, which may imply differences in the bonding character. The Ni and C atoms continue to show overlapping densities, maintaining a covalent nature. In contrast, Ni_3MgC presents a more uniformly spread electron density around the Mg atom, indicating weaker metallic bonding, while still retaining the covalent bonding between Ni and C atoms. These differences in electron density distributions among the three compounds suggest variations in the nature and strength of both metallic and covalent bonds, influenced by the type of central metal atom.

3.2. Phonon and electron–phonon interaction of Ni_3AC

The analysis of phonon dispersion, total and partial vibrational density of states (VDOS), and electron–phonon spectral function for Ni_3AC (A: Mg, Zn and Cd) have been studied because they play a crucial role in superconductivity. Thus the calculated phonon dispersion, total and partial phonon density of states and electron–phonon spectral function for Ni_3AC (A: Mg, Zn and Cd) are shown in Fig. 4(a–c), respectively. All three materials have 5 atoms per primitive unit cell, so there are 3 acoustic and 12 optical phonon modes. The presence of exclusively positive branches in the phonon spectrum signifies the dynamical stability of each compounds. As we can see from phonon spectrum in Fig. 4(a–c), due to mass differences there is separation region between branches distinctly: Low-frequency region (LFR) and high-frequency region (HFR). In the spectra of Ni_3MgC, the low-frequency region extends up to 10.0 THz, including eleven phonon branches, one of which is localized flat band around 8 THz in Fig. 4(a). This first region which is splitted from high-frequency region with a gap width of 6.0 THz from 16 THz to 20 THz contains 4 optical modes. The LFR of Ni_3ZnC and Ni_3CdC shows that lattice vibrations appear between 0 THz and 12.0 THz, and between 0 THz and 10.0 THz, with gap ranges of 7.0 THz and 6.0 THz, in Fig. 4(b) and Fig. 4(c), respectively. The HFR of Ni_3ZnC and Ni_3CdC lies between 18.0 THz and 22.0 THz, and 16.0 THz and 20.0 THz, respectively.

The flat phonon mode around 8 THz in Ni_3MgC is indeed indicative of an Einstein-like mode. This mode is characterized by localized vibrations primarily associated with the Mg atoms within the antiperovskite structure. In this structure, Mg occupies the central position in the cubic unit cell, surrounded by Ni atoms. The relatively flat nature of this mode suggests that the vibrations are localized and non-dispersive, which is typical of modes where atomic vibrations are weakly coupled to neighboring cells.
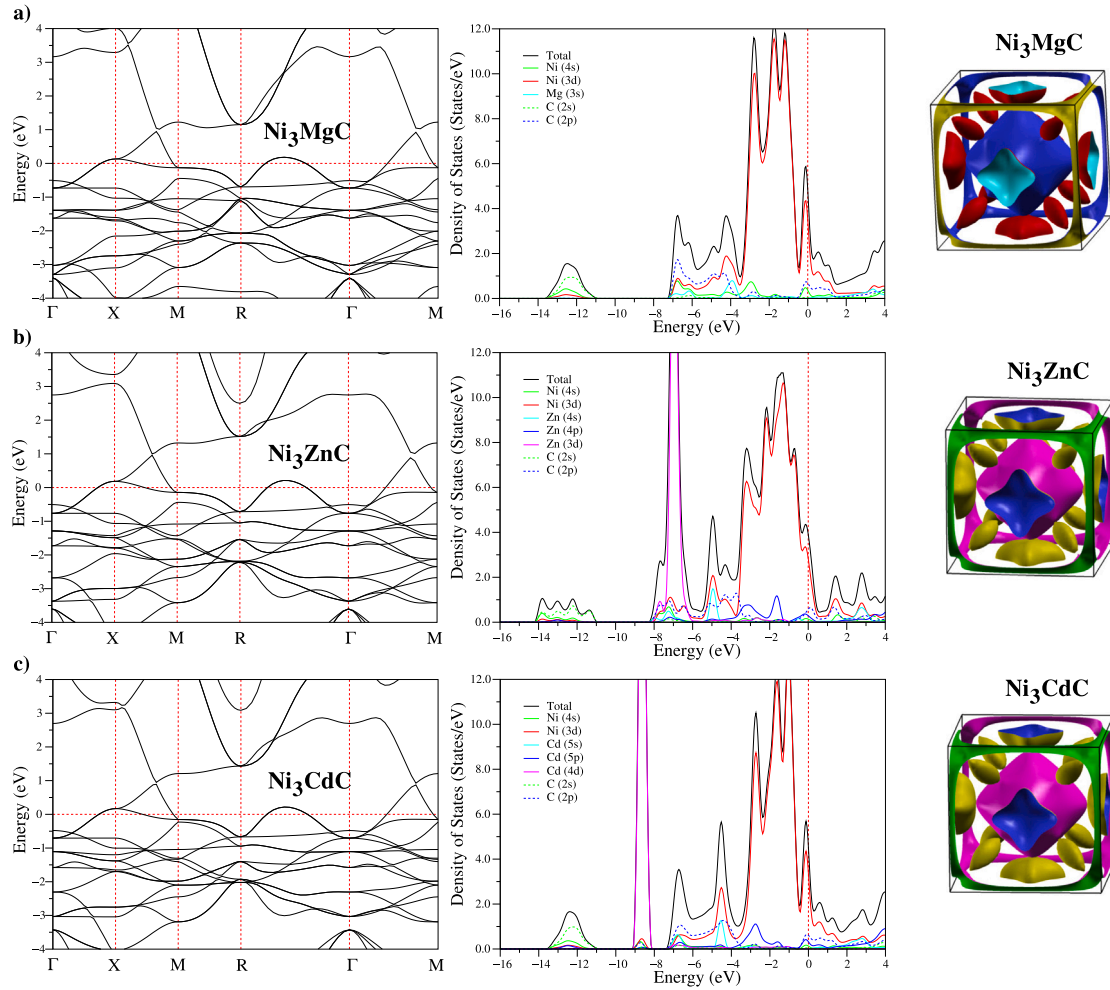
Fig. 2. The calculated electronic structure, partial, total DOS and Fermi surface plot of Ni₃MgC (a), Ni₃ZnC (b), and Ni₃CdC (c).
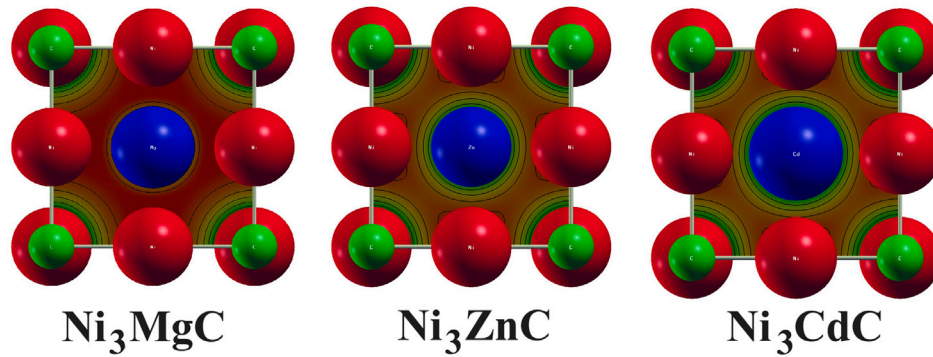

Fig. 3. The charge density distribution maps of Ni₃AC (A: Mg, Zn and Cd).

This mode's character is closely tied to the crystal structure, where the weaker bonding between Mg and Ni leads to these localized vibrations. The Mg atoms, due to their heavier mass and the weaker bonding environment, exhibit less interaction with surrounding atoms, resulting in the flatness of the mode in the phonon spectrum. This structural feature directly influences the thermal properties of Ni₃MgC, as such localized modes can reduce thermal conductivity by limiting the effective transport of vibrational energy across the crystal. Ni₃MgC contrasts with Ni₃ZnC and Ni₃CdC, where the phonon modes shift to lower frequencies with Zn and Cd, respectively, reflecting their heavier masses and further weakened bonding, resulting in even more localized

vibrations and likely reduced thermal conductivities in these heavier antiperovskites.

An in-depth study of the phonon density of states is necessary to identify the atoms responsible for the vibrations in Ni₃AC (A: Mg, Zn, and Cd). In the low-frequency range (0 to 7.0 THz), the vibrations of Ni atoms are the most significant contribution to the total phonon density of states. In Fig. 4(a), the flat band in the phonon dispersion near 8.0 THz causes a peak in the total density of states, with Mg atoms playing a significant role. However, this results in only minimal changes to the electron–phonon coupling parameter. This is already expected result, as Mg does not contribute to the electronic density
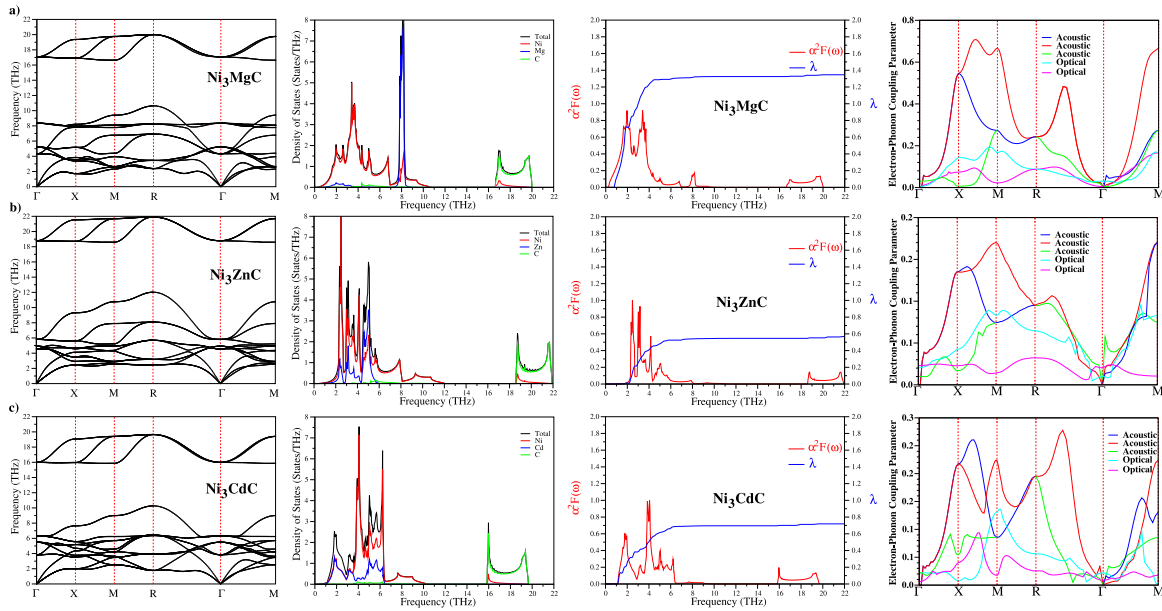
Fig. 4. The calculated phonon dispersion, phonon DOS, Eliashberg spectral function and the wave-vector dependence of the electron–phonon coupling parameter for the lowest acoustic branch of Ni_3AC (A: Mg, Zn and Cd).

Table 1
The density of states of Fermi level $N(E_F)$ (States/eV), the logarithmic frequency (ω_{ln}), the average electron–phonon coupling parameter (λ) and the superconducting transition temperature (T_c in K) for the antiperovskite Ni_3AC (A: Mg, Zn, and Cd) system and compared with previous theoretical results.

Material	$N(E_F)$ (States/eV)	ω_{ln} (K)	λ	T_c (K)
Ni_3MgC	**4.88**	**91.689**	**1.346**	**8.4**
Exp [4]				8.0
Exp [6]				6.7
Ni_3ZnC	**3.91**	**167.030**	**0.567**	**2.2**
Exp [6]				<2.0
Ni_3CdC	**4.52**	**134.311**	**0.719**	**3.9**
Exp [7]				3.2

of states much as we discussed in Fig. 4(a). In Ni_3AC (A: Mg, Zn and Cd), the electron–phonon interaction parameter rapidly increases in the low-frequency range. This indicates that these vibrations have a significant impact on how electrons scatter, more so than vibrations at higher frequencies. The density of states for Ni_3ZnC and Ni_3CdC indicates that the low-frequency range (LFR) is mainly dominated by the hybridization of Ni-Zn and Ni-Cd, as shown in Figs. 4(b) and 4(c), respectively. This is due to the strong covalent bonding between these atoms. In the high-frequency region, the phonon density of states is predominantly contributed by C atoms, as expected due to their lighter mass, with a smaller contribution from Ni atoms. The differences in the phonon density of states among Ni_3AC (A = Mg, Zn, Cd) are primarily due to the varying atomic masses of element A, which shift vibrational modes to lower frequencies for heavier elements, while the similarities stem from the consistent contribution of Ni-3d states, with the shift to higher frequencies in Ni_3ZnC due to stronger Zn-C bonding restricting carbon atom movement. Lighter elements like Mg contribute to higher frequency phonon modes due to their lower atomic mass, which can be favorable in maintaining dynamical stability and higher electron–phonon coupling in superconductors. The flat phonon mode observed around 8 THz in Ni_3MgC indicates localized vibrations that are less dispersive, which can positively impact superconducting properties.

The interaction between electrons and phonons can be analyzed using the linear response theory within the Migdal–Eliashberg theory. The total electron–phonon coupling constant (λ) can be determined by analyzing the Eliashberg spectral function ($\alpha^2 F(\omega)$), as given in Table 1. The electron–phonon coupling parameter (λ) is predominantly determined by contributions from the lowest frequency range, as shown in

Fig. 4. This contribution, comprising 96%, 92%, and 91%, respectively, mainly comes from the coordinated motion of Ni and A (Zn, Cd) atoms. In Ni_3MgC, the contribution of Mg is nearly negligible up to 6 THz, with the dominant contribution in this frequency range originating from the Ni atoms. In contrast, the contribution from the high-frequency region, predominantly influenced the lighter C atom modes, is negligible. Using the electron–phonon coupling parameter (λ), the logarithmic average phonon frequency (ω_{ln}) is determined to be 91.689, 167.030, and 134.311 K for Ni3AC (A: Mg, Zn, and Cd) respectively. The discrepancy between the shape of the Eliashberg spectral function and the phonon density of states (DOS) is indeed notable, particularly with the absence of contribution from the Mg-Ni mode around 8 THz. This observation indicates that not all phonon modes contribute equally to the electron–phonon coupling, as seen by the selectiveness in which some Ni-dominated modes do not contribute, while others have significant contributions. To clarify the connection between the phonon softening of the lowest acoustic branch and electron–phonon interaction, the wave-vector dependence of the electron–phonon coupling parameter for this phonon branch is given in Fig. 4. As shown in Fig. 4, the acoustic branches highlighted in blue and red are dominant in the electron–phonon interaction for Ni_3AC (A: Mg, Zn, and Cd). The values of λ and ω_{ln} are then used to determine the superconducting transition temperature (T_c) using the Allen–Dynes modification of the McMillan formula. The calculated superconducting parameters are given in Table 1. The results for T_c demonstrate remarkable agreement with experimental results [4,6,7].

In conclusion, T_c values of Ni_3AC (A: Mg, Zn and Cd) is calculated as 8.4 K, 2.2 K and 3.9 K. These values are in good agreement with the

reported experimental values of 8.0, 2.0 and 3.0 K [4,6,7]. Finally, the strength of the electron–phonon interaction suggests medium-coupling superconductivity for Ni_3AC (A: Mg, Zn and Cd).

CRediT authorship contribution statement

T. Zafer: Writing – review & editing, Writing – original draft, Data curation, Conceptualization. **F. Kurtuluş:** Software, Visualization, Writing – review & editing. **R. Salimov:** Writing – review & editing, Data curation, Conceptualization. **E. Karaca:** Writing – review & editing, Supervision, Software, Methodology, Data curation, Conceptualization.

Declaration of competing interest

The authors declare that they have no known competing financial interests or personal relationships that could have appeared to influence the work reported in this paper.

Acknowledgments

Data availability

No data was used for the research described in the article.

References

[1] W. Xia, Y. Zhao, F. Zhao, K. Adair, R. Zhao, S. Li, R. Zou, Y. Zhao, X. Sun, Antiperovskite electrolytes for solid-state batteries, Chem. Rev. 122 (3) (2022) 3763–3819.

[2] N. Hoffmann, T.F. Cerqueira, J. Schmidt, M.A. Marques, Superconductivity in antiperovskites, NPJ Comput. Mater. 8 (1) (2022) 150.

[3] Y. Wang, H. Zhang, J. Zhu, X. Lü, S. Li, R. Zou, Y. Zhao, Antiperovskites with exceptional functionalities, Adv. Mater. 32 (7) (2020) 1905007.

[4] T. He, Q. Huang, A. Ramirez, Y. Wang, K. Regan, N. Rogado, M. Hayward, M. Haas, J. Slusky, K. Inumara, et al., Superconductivity in the non-oxide perovskite $MgCNi_3$, Nature 411 (6833) (2001) 54–56.

[5] A. Dong, G. Che, W. Huang, S. Jia, H. Chen, Z. Zhao, Synthesis and physical properties of $AlCNi_3$, Physica C: Supercond. 422 (1–2) (2005) 65–69.

[6] M.-S. Park, J. Giim, S.-H. Park, Y. Lee, S. Lee, E. Choi, Physical properties of $ZnCNi_3$: comparison with superconducting $MgCNi_3$, Supercond. Sci. Technol. 17 (2) (2003) 274.

[7] M. Uehara, T. Yamazaki, T. Kôri, T. Kashida, Y. Kimishima, I. Hase, Superconducting properties of $CdCNi_3$, J. Phys. Soc. Japan 76 (3) (2007) 034714.

[8] C. Li, W. Chen, F. Wang, S. Li, Q. Sun, S. Wang, Y. Jia, First-principles investigation of mechanical and electronic properties of $MNNi_3$ (M=Zn, Mg, or Cd), J. Appl. Phys. 105 (12) (2009).

[9] P. Tong, Y. Sun, X. Zhu, W. Song, Strong electron-electron correlation in the antiperovskite compound $GaCNi_3$, Phys. Rev. B 73 (24) (2006) 245106.

[10] F. Saadaoui, F.Z. Driss Khodja, A.-E.-D. Kadoun, M. Driss Khodja, A. Elias, A. Boudali, First-principles calculations of structural, elastic, thermodynamic, and electronic properties of anti-perovskites A III CNi_3(A III=Al, Ga, In), Eur. Phys. J. B 88 (2015) 1–11.

[11] I. Shein, V. Bannikov, A. Ivanovskii, Structural, elastic and electronic properties of superconducting anti-perovskites MgCNi3, ZnCNi3 and CdCNi3 from first principles, Physica C: Supercond. Appl. 468 (1) (2008) 1–6.

[12] I. Shein, A. Ivanovskii, Electronic and elastic properties of non-oxide anti-perovskites from first principles: Superconducting $CdCNi_3$ in comparison with magnetic $InCNi_3$, Phys. Rev. B—Condens. Matter Mater. Phys. 77 (10) (2008) 104101.

[13] S. Bağcı, S. Duman, H.M. Tütüncü, G. Srivastava, Ground state, phonon spectrum, and superconducting properties of the nonoxide perovskite $CdCNi_3$, Phys. Rev. B—Condens. Matter Mater. Phys. 78 (17) (2008) 174504.

[14] M. Duan, J. Tan, G. Ji, X. Chen, J. Zhu, Elastic and thermodynamic properties of anti-perovskite type superconductor $MCNi_3$ (M=Zn, Cd), Acta Phys. Pol. A 118 (4) (2010) 652–658.

[15] H.M. Tütüncü, G. Srivastava, Electronic structure, phonons and electron–phonon interaction in $MgXNi_3$ (X=B, C and N), J. Phys.: Condens. Matter. 18 (49) (2006) 11089.

[16] J.-Y. Lin, P. Ho, H. Huang, P. Lin, Y.-L. Zhang, R.-C. Yu, C.-Q. Jin, H. Yang, BCS-like superconductivity in $MgCNi_3$, Phys. Rev. B 67 (5) (2003) 052501.

[17] R. Szcześniak, A. Durajski, et al., Thermodynamic properties of antiperovskite MgCNi3 in superconducting phase, Solid State Commun. 203 (2015) 63–68.

[18] R. Szcześniak, A. Durajski, K. Skoczylas, Ł. Herok, Low-temperature thermodynamic properties of superconducting antiperovskite $CdCNi_3$, J. Low Temp. Phys. 183 (5) (2016) 387–398.

[19] A. Wälte, G. Fuchs, K.-H. Müller, A. Handstein, K. Nenkov, V. Narozhnyi, S.-L. Drechsler, S. Shulga, L. Schultz, H. Rosner, Evidence for strong electron-phonon coupling in $MgCNi_3$, Phys. Rev. B—Condens. Matter Mater. Phys. 70 (17) (2004) 174503.

[20] P. Singer, T. Imai, T. He, M. Hayward, R. Cava, ^{13}C NMR investigation of the superconductor $MgCNi_3$ up to 800 K, Phys. Rev. Lett. 87 (25) (2001) 257601.

[21] J. Shim, S. Kwon, B. Min, Electronic structures of antiperovskite superconductors $MgXNi_3$ (X= B, C, and N), Phys. Rev. B 64 (18) (2001) 180510.

[22] P. Giannozzi, S. Baroni, N. Bonini, M. Calandra, R. Car, C. Cavazzoni, D. Ceresoli, G.L. Chiarotti, M. Cococcioni, I. Dabo, et al., QUANTUM ESPRESSO: a modular and open-source software project for quantum simulations of materials, J. Phys.: Condens. Matter. 21 (39) (2009) 395502.

[23] P. Giannozzi, O. Andreussi, T. Brumme, O. Bunau, M.B. Nardelli, M. Calandra, R. Car, C. Cavazzoni, D. Ceresoli, M. Cococcioni, et al., Advanced capabilities for materials modelling with quantum ESPRESSO, J. Phys.: Condens. Matter. 29 (46) (2017) 465901.

[24] A.M. Rappe, K.M. Rabe, E. Kaxiras, J. Joannopoulos, Optimized pseudopotentials, Phys. Rev. B 41 (2) (1990) 1227.

[25] W. Kohn, L.J. Sham, Self-consistent equations including exchange and correlation effects, Phys. Rev. 140 (4A) (1965) A1133.

[26] H.J. Monkhorst, J.D. Pack, Special points for brillouin-zone integrations, Phys. Rev. B 13 (12) (1976) 5188.

[27] A. Migdal, Interaction between electrons and lattice vibrations in a normal metal, Sov. Phys.—JETP 7 (6) (1958) 996–1001.

[28] G. Eliashberg, Interactions between electrons and lattice vibrations in a superconductor, Sov. Phys.—JETP 11 (3) (1960) 696–702.

[29] P.B. Allen, R. Dynes, Transition temperature of strong-coupled superconductors reanalyzed, Phys. Rev. B 12 (3) (1975) 905.

[30] P. Allen, R. Dynes, Superconductivity at very strong coupling, J. Phys. C: Solid State Phys. 8 (9) (1975) L158.